

1 **Structural, optical and photovoltaic properties of V<sub>2</sub>O<sub>5</sub>/ZnO and reduced graphene**  
2 **oxide (rGO)-V<sub>2</sub>O<sub>5</sub>/ZnO nanocomposite photoanodes for dye-sensitized solar cells**

3  
4 **C. Bhagya Lakshmi <sup>a,\*</sup>, S. Anna Venus <sup>a,\*</sup>, S. Velanganni <sup>b</sup>,**

5 **A. Muthukrishnaraj <sup>c</sup>, Manikandan Ayyar <sup>d, e, f,\*</sup> and Mohamed Henini <sup>g,h,i</sup>**

6  
7 <sup>a</sup>Energy Research Centre, Department of Physics, St. Xavier's College (Autonomous) affiliated  
8 to Manonmanium Sundaranar University, Tirunelveli, Palayamkottai-627002, India.

9 <sup>b</sup>Department of Chemistry, Parvathy's Arts and Science College (affiliated to Madurai Kamaraj  
10 University), Dindigul-624 002 India.

11 <sup>c</sup>Department of Chemistry, Faculty of Engineering, Karpagam Academy of Higher  
12 Education, Coimbatore - 641021, Tamil Nadu, India

13 <sup>d</sup>Department of Chemistry, Karpagam Academy of Higher Education,  
14 Coimbatore - 641021, Tamil Nadu, India

15 <sup>e</sup>Centre for Material Chemistry, Karpagam Academy of Higher Education,  
16 Coimbatore - 641021, Tamil Nadu, India

17 <sup>f</sup>Department of Chemistry, Bharath Institute of Higher Education and Research (BIHER),  
18 Chennai – 600 073, Tamil Nadu, India

19 <sup>g</sup>UNESCO UNISA Africa Chair in Nanosciences & Nanotechnology, College of Graduate  
20 Studies, University of South Africa, Muckleneuk Ridge, PO Box 392, Pretoria, South Africa

21 <sup>h</sup>Nanosciences African Network (NANO-AFNET), iThemba LABS-National Research  
22 Foundation, 1 Old Faure Road, Somerset West, PO Box: 722, Cape Town, 7129,  
23 South Africa

24 <sup>i</sup>School of Physics and Astronomy, University of Nottingham, Nottingham, NG7 2RD,  
25 United Kingdom

26  
27 \* **Corresponding Authors Email id:** [bhagya.jey@gmail.com](mailto:bhagya.jey@gmail.com) (C. Bhagya Lakshmi);  
28 [annavenus@stxavierstn.edu.in](mailto:annavenus@stxavierstn.edu.in) (S. Anna Venus); [manikandan.frsc@gmail.com](mailto:manikandan.frsc@gmail.com) (Manikandan  
29 Ayyar).

## 32 **Abstract**

33 Photoanode optimization is a fascinating technique for enlightening the **power conversion**  
34 **efficiency (PCE)** of dye-sensitized solar cells (**DSSCs**). In this present study,  $V_2O_5/ZnO$  and  
35 **reduced graphene oxide (rGO)- $V_2O_5/ZnO$  nanocomposites (NCs)** were prepared by the solid-  
36 state mixture technique and used as photoanodes for DSSCs. A wet chemical technique was  
37 implemented to generate individual  $V_2O_5$  and **ZnO nanoparticles (NPs)**. The structural  
38 characteristics of **the as-synthesized NCs** were investigated and confirmed **using powder X-**  
39 **ray diffraction (XRD), X-ray photoelectron spectra (XPS), and Scanning electron microscope**  
40 **(SEM) with energy dispersive X-ray (EDX) analysis.** The average crystallite size (D) of the  
41 **as-synthesized  $V_2O_5/ZnO$  and rGO- $V_2O_5/ZnO$  NCs** was determined by Debye-Scherrer's  
42 **formula.** The bandgap (eV) energy was calculated from Tauc's plots, and the bonding nature  
43 **and detection of the excitation of electrons** were investigated using the Ultra violet (UV)  
44 **visible spectra, Fourier Transform infrared (FTIR) and photoluminescence (PL) spectral**  
45 **analysis.** Electrical studies like Hall effect analysis and the Nyquist plots are also described.  
46 The  $V_2O_5/ZnO$  and rGO- $V_2O_5/ZnO$  NCs based DSSCs exhibited 0.64% and 1.27% of PCE  
47 and the short circuit current densities and open circuit voltages improved from **7.10 mA /cm<sup>2</sup>**  
48 **to 11.28 mA /cm<sup>2</sup>** and from **0.57 V to 0.68 V**, respectively.

49

50 **Keywords:** ZnO; Nanocomposites; Graphene Oxide; XPS spectrum; Dye-sensitized solar  
51 cells.

52

## 53 **1. Introduction**

54 Recently, dye-sensitized solar cells (DSSCs) can be seen as a talented alternate to the  
55 conservative photovoltaic strategies and has fascinated significant consideration as they offer  
56 the opportunity for low-cost and also high alteration **photovoltaic (PV) energy [1-3].** Over the

57 last decade, researchers have concentrated on developing a photoanode (working electrode)  
58 with a diversity of morphologies in order to expand the proficiency of DSSCs. TiO<sub>2</sub> is the  
59 greatest often active photoanode substantial in DSSCs, owing to its porosity and durable  
60 catalytic nature. Recently discovered interface properties such as charge departure, converse  
61 recombination, and tricking of photogenerated electrons in semiconductor device outsides  
62 self-sufficiently by defining optimal material mixtures and their gathering [4,5]. To maximize  
63 overall energy conversion efficiency (ECE), it is essential to construct a combination of  
64 materials consisting of various metal oxide semiconductors (MOS) that reduces  
65 recombination currents, improves light absorption, ensures a good electric connection.

66 Since of their low cost, eco-friendly stewardship, and significant production,  
67 carbonous materials are widely working to progress photocatalytic (PC) and photovoltaic  
68 (PV) activities. Recently, reduced graphene oxide (rGO) has been extensively employed as an  
69 active subsidiary material for attractive charge transfer and adsorption capacities owing to its  
70 exceptional attributes such as superior electrical conductivity (EC), high surface area and also  
71 good optical properties. Additionally, the combination of rGO with metal oxides can provide  
72 numerous advantages, including increased performance rate, longer cyclability, and higher  
73 sulphur consumption rates [6,7]. Metal oxide/rGO NCs are believed to be an important  
74 approach towards broadening the possibilities of MOS in fields such as energy gathering,  
75 alteration, and loading devices. Various kinds of MOS including rGO-TiO<sub>2</sub>, rGO-V<sub>2</sub>O<sub>5</sub>, rGO-  
76 ZnO, rGO-SnO<sub>2</sub>, and rGO-Nb<sub>2</sub>O<sub>5</sub>, etc. have been reported [8].

77 The various V<sub>2</sub>O<sub>5</sub> based attached semiconductors, including V<sub>2</sub>O<sub>5</sub>/BiVO<sub>4</sub>, V<sub>2</sub>O<sub>5</sub>/SiO<sub>2</sub>,  
78 TiO<sub>2</sub>/V<sub>2</sub>O<sub>5</sub>, V<sub>2</sub>O<sub>5</sub>/ZnO Au/V<sub>2</sub>O<sub>5</sub>/ZnO, Ag<sub>2</sub>O/V<sub>2</sub>O<sub>5</sub>/TiO<sub>2</sub>, RGO/V<sub>2</sub>O<sub>5</sub> and carbon  
79 nanostructures/V<sub>2</sub>O<sub>5</sub>, have been successfully synthesized in recent years [9-16]. Recently,  
80 Saravanan *et al.* reported photocatalytic (PCD) property of V<sub>2</sub>O<sub>5</sub>/ZnO NCs synthesized by  
81 hydrothermal route [12]. Yin *et al.* reported the synthesis and plasmonic PCD activity of Au-

82 decorated  $V_2O_5@ZnO$  materials [13]. Boruah *et al.* studied the  $Fe_3O_4@V_2O_5/rGO$  NCs as  
83 environmental photocatalyst [15].

84 In this perspective, it is desirable to study the photovoltaic (PV) behavior of rGO-  
85  $V_2O_5/ZnO$  NCs. Herein, for the first time we introduce the synthesis of  $V_2O_5/ZnO$  and rGO-  
86  $V_2O_5/ZnO$  NCs as photoanode material and fabricated a DSSC cell. Therefore, rGO-  
87  $V_2O_5/ZnO$  NCs may provide a new generation of materials for outstanding PV activity [16-  
88 20]. In the current study, we describe the solid-state reaction mixture method used to  
89 synthesize  $V_2O_5/ZnO$  and rGO- $V_2O_5/ZnO$  NCs. We have investigated physical and chemical  
90 properties using XRD, SEM with EDX, XPS, UV-Vis, FT-IR, PL spectra, Hall effect and  
91 impedance analysis. The photovoltaic (PV) performance of  $V_2O_5/ZnO$  and rGO- $V_2O_5/ZnO$   
92 NCs integrated photoanode in DSSCs was assessed under ordinary simulated sun light  
93 intensity of  $100\text{ mW}\cdot\text{cm}^{-2}$ .

94

## 95 **2. Experimental details**

### 96 **2.1 Materials**

97 As precursors, cetyl trimethyl ammonium bromide (CTAB), sodium metavanadate,  
98 ammonium chloride ( $NH_4Cl$ ), zinc nitrate, sodium hydroxide, rGO and ethanol solution are  
99 employed. The materials are purchased in Hi-media AR grade used without additional  
100 purification. Pilkington provided indium doped tin oxide glass plates (TEC7) with resistance  
101 of  $15\text{-}25\ \Omega/\text{cm}^2$ . N719 dye was acquired from Sigma-Aldrich. For sample preparation and  
102 washings, double deionised (DD) water was used.

103

### 104 **2.2 Characterization techniques**

105 Crystalline structure of  $V_2O_5/ZnO$  and rGO- $V_2O_5/ZnO$  NCs were characterized by PAN  
106 analytical X'PERT PRO diffractometer (Cu K $\alpha$  radiation,  $k = 1.54\text{\AA}$ ). Scanning electron

107 microscopy (JEOL - JSM 5610LV) coupled with an energy-dispersive X ray (EDX) analyser  
108 was used to investigate the morphology and elemental compositions of the as-prepared  
109 composites. The ULVAC-PHI X-Ray photoelectron spectrometer was employed for XPS  
110 analysis (PHI5000). The FTIR spectrum was obtained using a Perkin Elmer Spectrum Two  
111 instrument with a range of 4000  $\text{cm}^{-1}$  to 400  $\text{cm}^{-1}$ . Shimadzu model spectrometer was used to  
112 record the UV-Visible spectrum. The PL spectrum was measured with a Shimadzu RF-  
113 5301PC spectro-fluorophotometer. Ecopia HMS-7000 Photonic Hall Effect Measurement  
114 System was used to determine electrical properties such as carrier concentration (n), mobility  
115 ( $\mu$ ), resistivity ( $\rho$ ) and conductivity ( $\sigma$ ). Hioki IM3536 General Purpose LCR Meter, DC 4  
116 Hz to 8 MHz, was used to measure the impedance (ratio of Voltage to Current (V/I))  
117 value. Photo Emission Technology solar simulator from Newport (Oriel QEPVSI-B  
118 IPCE System) was used for current-voltage characterization studies.

119

### 120 *2.3 Synthesis of $\text{V}_2\text{O}_5$ and ZnO nanoparticles*

121 The synthesis of **vanadium penta oxide ( $\text{V}_2\text{O}_5$ ) and zinc oxide (ZnO) nanoparticles (NPs)**  
122 were prepared by chemical wet method. Initially, 100 ml of DD water with 8 mM sodium  
123 metavanadate fully dissolved was subjected to continual stirring. After that, the solution was  
124 thoroughly dissolved in 200 mM of  $\text{NH}_4\text{Cl}$ . After a few minutes, the solution's colour  
125 changed from murky to clear, then to smokey. Ten minutes later, 10 mM of Cetyl trimethyl  
126 ammonium bromide (CTAB) was included in the solution, and the temperature of the  
127 synthesis was elevated to 80 °C. Colour of the solution transformed from orange to dark  
128 brown. A transparent yellow colour appeared in the solution after an hour. The final product  
129 was dried for 4 hours, then permitted to cool to ambient temperature and calcinated for 4  
130 hours at 420 °C.

131 For preparation of ZnO NPs, 1.2 M of sodium hydroxide (NaOH) in aqueous ethanol  
132 solution and 0.7 M of zinc nitrate in aqueous ethanol solution were both stirred for an hour.  
133 The prepared NaOH aqueous solution was added dropwise to the zinc nitrate solution while  
134 being constantly stirred at high speed. The remaining sodium hydroxide was added, and the  
135 reaction was allowed to proceed for 2 hours. After being centrifuged for 10 minutes at 6000  
136 rpm, the solution was left to settle for a few hours. Thus, precipitated ZnO NPs were dried in  
137 a muffle furnace for 1 hour at 60 °C and the final product was then annealed at a temperature  
138 of 420 °C.

139

#### 140 *2.4 Synthesis of rGO-V<sub>2</sub>O<sub>5</sub>/ZnO nanocomposites*

141 The process of rGO-V<sub>2</sub>O<sub>5</sub>/ZnO NCs was carried out via standard solid-state reaction method.  
142 Prepared V<sub>2</sub>O<sub>5</sub> and ZnO NPs were mixed with rGO in various stoichiometric ratios. The  
143 mixture was extensively crushed in a mortar and pestle to obtain the best reaction activity and  
144 homogeneity. Ethanol was slightly added as a solvent to serve as a reaction medium. The  
145 combined mixture was heated at 450 °C for 6 hours in a muffle furnace and was eventually  
146 cooled to room temperature before being taken out. A schematic diagram of solid-state  
147 reaction method for the preparation is shown in **Figure 1**.

148

#### 149 *2.5 Fabrication of photoanodes*

150 The ITO glasses were cleaned in an ultrasonic water bath with acetone, ethanol, and DD  
151 water before being dried in hot air. The doctor blade technique was implemented to coat a  
152 photoanode consisting of prepared NCs (V<sub>2</sub>O<sub>5</sub>/ZnO and rGO-V<sub>2</sub>O<sub>5</sub>/ZnO). Before starting the  
153 slurry coating procedure, the necessary amount of rGO-V<sub>2</sub>O<sub>5</sub>/ZnO NCs powder and acetyl  
154 acetone is coarsely crushed in a mortar. ITO slides were coated with a fine slurry of rGO-  
155 V<sub>2</sub>O<sub>5</sub>/ZnO and dried in a muffle furnace for 30 minutes at 420 °C. The consistent approach

156 was employed to generate the V<sub>2</sub>O<sub>5</sub>/ZnO photoanodes. Dropping chloroplatinic hydrate acid  
157 on a conducting glass substrate and annealing it in air at 420 °C for 30 minutes resulted in the  
158 formation of a Pt electrode [21,22]. **Fig. 2** shows coated photoanodes made from V<sub>2</sub>O<sub>5</sub>/ZnO  
159 and rGO-V<sub>2</sub>O<sub>5</sub>/ZnO **NCs**.

160

## 161 **2.6 Fabrication of DSSCs**

162 In general, the produced photoanodes were immersed in a solution containing N719 dye for  
163 24 hours in a dark environment [23]. Following the dye adsorption, the substrates were rinsed  
164 with ethanol to remove excess dye and dried in hot air. Consequently, the DSSCs were  
165 fabricated by clipping together prepared photoanodes with Pt counter electrodes. The I<sup>-</sup> / I<sub>3</sub><sup>-</sup>  
166 redox electrolyte, which included NaI and I<sub>2</sub>, was injected into the DSSCs using a small  
167 syringe [24]. The calculated active regions of cells are 1.1 cm<sup>2</sup>. All the fabrication and  
168 characterization processes were carried out in an ambient atmosphere without any protective  
169 atmosphere.

170

## 171 **3. Results and discussions**

### 172 **3.1 XRD diffraction analysis**

173 **Fig. 3** shows the XRD pattern of as-synthesised V<sub>2</sub>O<sub>5</sub>, ZnO **NPs** and rGO -V<sub>2</sub>O<sub>5</sub>/ZnO **NCs**,.  
174 The V<sub>2</sub>O<sub>5</sub> individual peaks have 2θ values at 15.23°, 20.66°, 25.91°, 29.16°, 37.43°, 40.59°,  
175 43.12°, 44.19°, 45.53°, 46.10°, 49.20°, 51.73° and 57.3° equivalent to the planes (200), (001),  
176 (110), (301), (407), (311), (102), (202), (411), (510), (112), (212) and (121), respectively.  
177 This result reveals that V<sub>2</sub>O<sub>5</sub> phase (orthorhombic) is well aligned with standard data base of  
178 JCPDS card no: 77-2418. On the other hand, the observed 2θ peaks for ZnO of 32.29°,  
179 34.89°, 36.74°, 47.93°, 63.25°, 66.84°, 68.37° and 69.52° correspond to (100), (002), (101),  
180 (102), (103), (200), (112) and (201) planes, respectively, and are matched with JCPDS card

181 no 89-1397. The minor detected peaks at  $22.08^\circ$  and  $41.98^\circ$  are related to the (002) and (100)  
182 plane of rGO, respectively. Similar results were reported by Stobinski et al. [25]. The  
183 calculated average crystallite size (D) of the rGO -V<sub>2</sub>O<sub>5</sub>/ZnO is found to be 14.12 nm using  
184 Debye Scherrer's formula.

185

### 186 **3.2 SEM with EDX analysis**

187 The surface morphology and average particle size was examined by scanning electron  
188 microscopy (SEM) analysis (**Fig. 4**). V<sub>2</sub>O<sub>5</sub>/ZnO possess a cluster of spherical shaped  
189 materials with particle size of ~ 36.8 nm (**Fig. 4 a,b**) and it is also evident that there are very  
190 tiny group of small clusters stacked together with diameter of 13 nm to 25 nm spheres in the  
191 case of V<sub>2</sub>O<sub>5</sub>/ZnO/rGO (**Fig. 4 c,d**), which indicates the presence of rGO in the NCs. It is  
192 important to note that the average crystallite sizes results obtained from XRD are well  
193 matched with SEM images. From EDX analysis, it is confirmed that the as-prepared samples  
194 have no impurities and have 50.92 % of C, 22.65% of O, 17.37% of V and 9.06% of Zn for  
195 V<sub>2</sub>O<sub>5</sub> /ZnO/rGO NCs and for 24.45 % of O, 51.87 % of V and 23.67 % of Zn for V<sub>2</sub>O<sub>5</sub> /ZnO  
196 (**Fig. 5**) [26].

197

### 198 **3.3 XPS spectrum**

199 To probe the electronic structure and chemical environment, XPS spectra are investigated.  
200 All four elements (C, V,O and Zn) given by XPS scan are shown in **Fig. 6a**. The XPS  
201 spectrum for rGO - V<sub>2</sub>O<sub>5</sub> /ZnO NCs indicate the presence of C 1s at 284.8 eV- 289.1 eV, V  
202 2p at 517 eV - 535 eV, O 1s at 530.5 eV - 532.5 eV, and Zn 2p at 497 eV-1021 eV as  
203 illustrated in **Fig. 6a**.

204 The XPS scan for carbon content in the samples confirms the C 1s peaks (**Fig. 6b**) at  
205 284.8 eV, 286 eV and 289.1 eV. Furthermore, the XPS scan for vanadium shows peaks at



206 517.7 eV and 525 eV ascribed to V 2p<sub>3/2</sub> and V 2p<sub>1/2</sub>, respectively. The small minor peaks at  
207 530.5eV and 532.4eV of V 2p peaks confirm the presence of vanadium (**Fig. 6c**). In Zn 2p  
208 spectrum (**Fig. 6d**), Zn 2p<sub>3/2</sub> peak is observed at a binding energy of 1021.6 eV indicating the  
209 presence of Zn content. As shown in **Fig. 6e**, the high intensity peaks at 530.5 eV and 532.4  
210 eV are attributed to O 1s [27-29] and confirm the presence of oxygen.

211

### 212 **3.4 UV ViS Analysis**

213 The prepared rGO-V<sub>2</sub>O<sub>5</sub>/ZnO NCs have absorption in the visible and UV range of the light  
214 spectrum with an absorption edge at 582 nm, whereas the V<sub>2</sub>O<sub>5</sub>/ZnO NCs have UV light  
215 absorption edge between ~ 320 and 585 nm. From **Fig. 7a**, it is noticeable that absorption  
216 bands move towards the lower wavelength (blue shift) compared to rGO-V<sub>2</sub>O<sub>5</sub>/ZnO NCs. To  
217 find the conducting behavior, we have determined the bandgap energy (*E<sub>g</sub>*) of synthesized  
218 NCs. The *E<sub>g</sub>* values, which were calculated by plotting Taucs plot graphs, are found to be  
219 2.54 eV for V<sub>2</sub>O<sub>5</sub>/ZnO and 2.64 eV for rGO-V<sub>2</sub>O<sub>5</sub>/ZnO as shown in **Fig. 7b**.

220 rGO has an absorption edge at 256 nm (**Fig. 7a**) which agrees with the earlier report  
221 [8]. rGO-V<sub>2</sub>O<sub>5</sub>/ZnO absorption spectrum is wider compared to individual rGO and V<sub>2</sub>O<sub>5</sub>/ZnO  
222 nanomaterials. The inclusion of rGO clearly broadens the spectrum and leads to the red shift  
223 observed in absorbance in the range of ~250 nm (**Fig. 7a**). This confirms the presence of rGO  
224 in the prepared samples. Therefore, the increased bandgap and the observed wide absorption  
225 peaks indicate that the prepared NCs could have good photovoltaic behaviour. In both NCs  
226 we can see nearly the same cut-off wavelength but with a large difference in absorption  
227 coefficient. This also shows the significant role of rGO.

228

229

230

### 231 **3.5 FT-IR spectrum**

232 FT-IR spectrum for rGO-V<sub>2</sub>O<sub>5</sub>/ZnO NCs was recorded in the range of 400 – 4000 cm<sup>-1</sup> and is  
233 shown in **Fig. 8**. From the FTIR spectrum, various functional groups and metal oxide (MO)  
234 bonds present in the composite were analyzed. **The vibration bands observed in the ranges**  
235 **from 600-850 cm<sup>-1</sup>, which are attributed to the characteristic stretching modes of Zn-O and**  
236 **V=O bonds. The peaks at 622 cm<sup>-1</sup> (asymmetric stretching V-O-V), 835 cm<sup>-1</sup> (symmetric**  
237 **stretching, V-O), 1012 cm<sup>-1</sup> (symmetric stretching, V = O) and the peak were observed at 516**  
238 **cm<sup>-1</sup> indicated Zn-O band [30]. A tiny band at 2923 cm<sup>-1</sup> is due to C-H groups. A wide band**  
239 **at 3439 cm<sup>-1</sup> indicates the presence of hydroxyl residue [31, 32].**

240

### 241 **3.6 Photoluminescence (PL) spectrum**

242 **Photoluminescence (PL) spectra of the rGO-V<sub>2</sub>O<sub>5</sub>/ZnO NCs are shown in Fig. 9. The two**  
243 **typically sharp peaks observed at ~ 469 nm and 606 nm, correspond to near band edge (NBE)**  
244 **emission and deep level emission (DLE), respectively. A lower intensity of PL reveals low**  
245 **charge recombination. Both V<sub>2</sub>O<sub>5</sub>/ZnO NCs and rGO-V<sub>2</sub>O<sub>5</sub>/ZnO NCs exhibit approximately**  
246 **the same wavelength (nm) range but rGO-V<sub>2</sub>O<sub>5</sub>/ZnO NCs shows lowest intensity compared**  
247 **to the other, which suggests that there is electron-hole (e-h) pair recombination in the**  
248 **synthesized rGO-V<sub>2</sub>O<sub>5</sub>/ZnO. PL studies shows good agreement with UV-Vis studies and**  
249 **revealed that the synthesized NCs could be used in opto-electronic devices.**

250

### 251 **3.7 Electrical studies**

#### 252 **3.7.1 Hall effect analyses**

253 The electrical properties such as carrier concentration (n), mobility (μ), resistivity (ρ) and  
254 conductivity (σ) for the synthesized rGO-V<sub>2</sub>O<sub>5</sub>/ZnO NCs are studied using the Hall effect  
255 method and the results are shown in **Table 1**. From the earlier reports [33, 34], it is clear that

256 pure  $V_2O_5$  and ZnO possess n-type conductivity, while in case of rGO it behaves either as p-  
257 or n-type material depending on the temperature treatment. In this work, the Hall effect  
258 results reveal that the prepared nanocomposites exhibit n-type behaviour and the carrier  
259 concentration is found to be  $4.94 \times 10^{12} \text{ cm}^{-3}$ . Mobility is an important parameter to consider  
260 in assessing the performance of photovoltaic (PV) devices. A higher mobility will reduce the  
261 recombination of photo-generated charges and increases the efficiency of PV devices.

262

### 263 **3.7.2 Nyquist plots**

264 Electrochemical Impedance Spectroscopy (EIS) is used to generate Nyquist plots for  
265 investigating the charge transfer process and determining the values of resistance and  
266 capacitance of the devices. The characterization is analyzed in the frequency range of 100 Hz  
267 – 400000 Hz. Nyquist plots were drawn for real parts and imaginary parts of the impedance  
268 values in X and Y axis, respectively. The value of real impedance depicts the value of the  
269 resistance of the samples. The resistance of rGO- $V_2O_5$ /ZnO NCs, which can be analysed  
270 from the Nyquist plots by measuring the diameter of the semicircle (**Fig. 10**), was found to be  
271  $\sim 6500 \Omega$ . The higher resistance value will slow down the movement of electrons in this  
272 aspect and from earlier reports we can conclude that rGO- $V_2O_5$ /ZnO NCs have lower  
273 resistance values, which are revealed from the electrical studies. This finding confirms the  
274 enhanced photovoltaic (PV) behaviour of the rGO - $V_2O_5$ /ZnO NCs.

275

### 276 **3.8 Photoelectrochemical (PEC) Parameters**

277 Current density-Voltage (J-V) curves of the prepared  $V_2O_5$ /ZnO and rGO- $V_2O_5$ /ZnO  
278 photoanodes are (**Fig. 11**) measured under simulated  $100 \text{ mW/m}^2$  power generation. The fill  
279 factor (FF) and power conversion efficiency ( $\eta$ ) of fabricated DSSCs are estimated using the  
280 relation given by equations (1) and (2).

281

282 
$$FF = J_{max} \cdot V_{max} / J_{sc} \cdot V_{oc} \dots\dots\dots (1)$$

283 where,  $J_{max}$  is the maximum current density,  $V_{max}$  is the maximum voltage,  $J_{sc}$  is the short-  
284 circuit current,  $V_{oc}$  is the open-circuit voltage and  $P_{in}$  is the power of incident light. Power  
285 conversion efficiency (PCE) was determined using equation 2

286 
$$\eta = J_{sc} \cdot V_{oc} \cdot FF / P_{in} \cdot 100\% \dots\dots\dots (2)$$

287 From **Fig. 11**, it can be observed that rGO-V<sub>2</sub>O<sub>5</sub>/ZnO photoanodes exhibit higher device  
288 performance than V<sub>2</sub>O<sub>5</sub>/ZnO photoanodes. The cells based on rGO-V<sub>2</sub>O<sub>5</sub> /ZnO photoanodes  
289 show an enhanced PEC values which are tabulated in **Table 2**. The work function of reduced  
290 graphene is sufficient for charge separation, and addition of rGO can increase the electrical  
291 conductivity of photoanodes [35, 36]. Thus, the rGO serves as the electron acceptor and  
292 facilitate rapid transport of photo generated electrons, thereby decreases the e-h  
293 recombination rates [37-40]. The lower power conversion efficiency (PEC) values for  
294 V<sub>2</sub>O<sub>5</sub>/ZnO photoanodes may be due to less conduction path between anodes and low dye  
295 loading behaviour. Furthermore, adding rGO enhances the efficiency of DSSCs, which can  
296 be evidently proved by electrical analysis and J-V curves. **Table 3. Various Photoanode**  
297 **materials and their photoconversion efficiencies.** Though various photoanodes with higher  
298 efficiency have been reported earlier, rGO-V<sub>2</sub>O<sub>5</sub>/ZnO NCs as photoanodes for DSSCs have  
299 been successfully fabricated for the first time and reported in this work. DSSCs with V<sub>2</sub>O<sub>5</sub>  
300 /ZnO exhibit a short-circuit current density of 4.02 mA/cm<sup>2</sup>, an open-circuit voltage of 0.245  
301 V, fill factor of 0.72 % and overall efficiency as 0.71 %.

302

303 **4. Conclusions**

304 **In summary, a solid-state reaction method was used for the synthesis of rGO-V<sub>2</sub>O<sub>5</sub>/ZnO and**  
305 **V<sub>2</sub>O<sub>5</sub>/ZnO NCs as photoanodes in DSSCs which were successfully fabricated and**

306 characterized. Powder XRD, SEM with EDX, XPS and FTIR results confirmed the  
307 successful formation of the NCs. Morphological analysis revealed the uniform formation of  
308 rGO-V<sub>2</sub>O<sub>5</sub>/ZnO and V<sub>2</sub>O<sub>5</sub>/ZnO NCs with average particle size around 13~25 nm and 20-60  
309 nm, respectively. The Tauc's plots revealed a bandgap energy of 3.14 eV and provided  
310 evidence that the inclusion of rGO made the absorption spectrum wider, caused a red shift  
311 obtained in the UV-Vis absorbance, and introduced changes in the charge transfer behaviour  
312 of photovoltaic (PV) process. In addition, the incorporation of rGO in the V<sub>2</sub>O<sub>5</sub>/ZnO NCs  
313 improved the PCE parameters such as open-circuit voltage, short-circuit current density, FF  
314 and efficiency of fabricated DSSCs. The low resistance and carrier concentration values and  
315 high mobility nature further helped for the enhancement of the photovoltaic (PV)  
316 performances. Overall, the structural, optical and electrical results for the prepared rGO-  
317 V<sub>2</sub>O<sub>5</sub>/ZnO NCs indicate that high performance photovoltaic (PV) devices can be achieved.

318

### 319 **Declaration of Competing Interest**

320 The authors declare that they have no known competing financial interests or personal  
321 relationships that could have appeared to influence the work reported in this paper.

322

### 323 **Acknowledgement**

324 The authors would like to extend their gratitude to Tamil Nadu State Council for Science &  
325 Technology - RFRS 19-20 for the financial support of the work.

326

### 327 **References**

328 [1] Chris J. Barnett, Alvin Orbaek White, Andrew R. Barron, Size dependent conduction  
329 characteristics of catalyst-multi-walled carbon nanotube junction, Carbon Letters, 31 (2021)  
330 1015–1021.

- 331 [2]. Majid Shaker, Ali Asghar Sadeghi Ghazvini, Faisal Raza Qureshi, Reza Riahifar, A  
332 criterion combined of bulk and surface lithium storage to predict the capacity of porous  
333 carbon lithium-ion battery anodes: lithium-ion battery anode capacity prediction, *Carbon*  
334 *Letters*, 31 (2021) 985–990.
- 335 [3]. M. Infant Shyam Kumar, S. Shahil Kirupavathy, S. Shalini, Exploration on reduced  
336 graphene oxide/strontium pyro niobate electrode material for electrochemical energy storage  
337 applications, *Carbon Letters* 31(2021) 619–633.
- 338 [4]. F. Asghar, Babar Murtaza, Bushra Shakoor, Nabtahil Iqbal, Maria Shafique, Rafia  
339 Murtaza, Ian Sydney Butler, Properties, assembly and characterization of carbon nanotubes:  
340 their application in water purification, environmental pollution control and biomedicines-a  
341 comprehensive review. *Carbon Letters* 33 (2023) 275–306.
- 342 [5]. H. Medetalibeyoğlu, An investigation on development of a molecular imprinted sensor  
343 with graphitic carbon nitride (g-C<sub>3</sub>N<sub>4</sub>) quantum dots for detection of acetaminophen. *Carbon*  
344 *Letters* 31 (2021) 1237–1248.
- 345 [6]. S. Akash Prabhu, V. Kavithayeni, R. Suganthy, K. Geetha, Graphene quantum dots  
346 synthesis and energy application: a review. *Carbon Letters* 31 (2021) 1–12.
- 347 [7]. T. Khac Le, M. Kang, V. Tam Tran, Sok Won Kim, Relation of photoluminescence and  
348 sunlight photocatalytic activities of pure V<sub>2</sub>O<sub>5</sub> nanohollows and V<sub>2</sub>O<sub>5</sub>/RGO nanocomposites,  
349 *Materials Science in Semiconductor Processing* 100 (2019) 159–166
- 350 [8]. Xin An, Guannan Xing, Jing Wang, Yanhong Tian, Yunfang Liu, Qiong  
351 Wan, Preparation of activated carbon spheres and their electrochemical properties as  
352 supercapacitor electrode, *Carbon Letters* 31 (2021) 667–676.
- 353 [9]. J. Su, X. Xin Zou, G. Dong Li, X. Wei, C. Yan, Yu-Ning Wang, J. Zhao, Li-Jing Zhou,  
354 Jie-Sheng Chen, Macroporous V<sub>2</sub>O<sub>5</sub>BiVO<sub>4</sub> Composites: Effect of Heterojunction on the  
355 Behavior of Photogenerated Charges, *J. Phys. Chem. C* 115 (2011) 8064–8071.

- 356 [10]. F. Amano, T. Tanaka, Takuzo Funabiki, Steady-State Photocatalytic Epoxidation of  
357 Propene by O<sub>2</sub> over V<sub>2</sub>O<sub>5</sub>/SiO<sub>2</sub> Photocatalysts, *Langmuir* 20 (2004) 4236–4240.
- 358 [11]. L. Jianhua, Y. Rong, L. Songmei, Synthesis and photocatalytic activity of TiO<sub>2</sub>/V<sub>2</sub>O<sub>5</sub>  
359 Composite Catalyst Doped with Rare Earth Ions, *J. Rare Earths* 25 (2007) 173–178.
- 360 [12]. R. Saravanan, V.K. Gupta, Edgar Mosquera, F. Gracia, Preparation and characterization  
361 of V<sub>2</sub>O<sub>5</sub>/ZnO nanocomposite system for photocatalytic application, *Journal of Molecular*  
362 *Liquids*. 198, (2014) 409-412.
- 363 [13]. H. Yin, K. Yu, C. Song, R. Huang, Z. Zhu, Synthesis of Au-decorated V<sub>2</sub>O<sub>5</sub>@ZnO  
364 heteronanostructures and enhanced plasmonic photocatalytic activity, *ACS Appl.Mater.*  
365 *Interfaces* 6 (2014) 14851–14860.
- 366 [14]. Y. Wang, L. Liu, L. Xu, X. Cao, X. Li, Y. Huang, C. Meng, Z. Wang, W. Zhu,  
367 Ag<sub>2</sub>O/TiO<sub>2</sub>/V<sub>2</sub>O<sub>5</sub> one-dimensional nanoheterostructures for superior solar light photocatalytic  
368 activity, *Nanoscale* 6 (2014) 6790.
- 369 [15]. P.K. Boruah, S. Szunerits, R. Boukherroub, M.R. Das, Magnetic Fe<sub>3</sub>O<sub>4</sub>@V<sub>2</sub>O<sub>5</sub>/rGO  
370 nanocomposite as a recyclable photocatalyst for dye molecules degradation under direct  
371 sunlight irradiation, *Chemosphere* 191 (2018) 503–513.
- 372 [16]. E. Aawani, N. Memarian, H.R. Dizaji, Synthesis and characterization of reduced  
373 graphene oxide–V<sub>2</sub>O<sub>5</sub> nanocomposite for enhanced photocatalytic activity under different  
374 types of irradiation, *J. Phys. Chem. Solids* 125 (2019) 8–15.
- 375 [17]. Majid Farahmandjou, Nilofer abaeiyan, Chemical Synthesis of Vanadium Oxide (V<sub>2</sub>O<sub>5</sub>)  
376 Nanoparticles Prepared by Sodium Metavanadate, *Journal of Nanomedicine Research* (2017),  
377 5(1): 00103.
- 378 [18]. Peng Li, Xiaoxiao Ma, Yurong Liang, Junhua Tan, Liyong Wang, Preparation and  
379 electrochemical capacitive properties of C–MnO<sub>2</sub> composite with foam-like structure based  
380 on modified rubber. *Carbon Lett.* 29, (2019) 547–552.

381 [19]. Sujin Seok, Dawoon Jang, Haeju Kim, Sungjin Park, Production of NiO/N-doped  
382 carbon hybrid and its electrocatalytic performance for oxygen evolution reactions. *Carbon*  
383 *Lett.* 30 (2020) 485–491.

384 [20]. Y. Ma, Yanli Liu, Preparation of graphene-ZnO composite with enhanced  
385 photocatalytic performance. *Carbon Lett.* 32 (2022) 1265–1275.

386 [21]. Ragu Sasikumar, Tse-Wei Chena, Shen-Ming Chena, Syang-Peng Rweib, Sayee  
387 Kannan Ramaraj, Developing the photovoltaic performance of dye-sensitized solar cells  
388 (DSSCs) using a SnO<sub>2</sub>-doped graphene oxide hybrid nanocomposite as a photo-anode,  
389 *Optical materials* 79 (2018) 348-352.

390 [22]. Palraj Ranganathan, Ragu Sasikumar, Shen-Ming Chen, Syang-Peng Rwei, Pedaballi  
391 Sireesha, Enhanced photovoltaic performance of dye-sensitized solar cells based on nickel  
392 oxide supported on nitrogen-doped graphene nanocomposite as a photoanode, *Journal of*  
393 *colloid and interface science* 504 (2017) 570-578.

394 [23]. P Sireesha, R Sasikumar, Shen-Ming Chen, Chaochin Su, Palraj Ranganathan, Syang-  
395 Peng Rwei, Carboxylic acid-functionalized multi-walled carbon nanotubes-polyindole/Ti<sub>2</sub>O<sub>3</sub>,  
396 A novel hybrid nanocomposite as highly efficient photo-anode for dye-sensitized solar cells  
397 (DSSCs), *Applied Surface Science* 423 (2017) 147–153.

398 [24]. Vignesh Murugadoss, Ning Wang, Sruthi Tadakamalla, In-Situ Grown Cobalt  
399 Selenide/Graphene Nanocomposites Counter Electrode for Enhanced Dye-sensitized Solar  
400 Cell Performance, *Journal of materials chemistry A*, (2017) 14583–14594.

401 [25]. L. Stobinski, B. Lesiak, A. Malolepszy, M. Mazurkiewicz, B. Mierzwa, J. Zemek, P.  
402 Jiricek, I. Bieloshapka, Graphene oxide and reduced graphene oxide studied by the XRD,  
403 TEM and electron spectroscopy methods, *Journal of Electron Spectroscopy and Related*  
404 *Phenomena* 195 (2014) 145–154.



405 [26]. Majid Azarang, Ahmad Shuhaimi and M. Sookhikian, Crystalline quality assessment,  
406 photocurrent response and optical properties of reduced graphene oxide uniformly decorated  
407 zinc oxide nanoparticles based on the graphene oxide concentration, RSC Adv., 5 (2015)  
408 53117.

409 [27]. Sandhya Venkateshalu, Jayesh Cherusseri, Manickavasakam Karnan, Kowsik Sambath  
410 Kumar, New Method for the Synthesis of 2D Vanadium Nitride (MXene) and Its Application  
411 as a Supercapacitor Electrode, ACS omega 5, 29, (2020) 17983–17992.

412 [28]. C. Bhagya Lakshmi, S. Jayalakshmi, S. Annavenus, Exploring CuBiSe/Y<sub>2</sub>O<sub>3</sub>  
413 Nanocomposite Material as a Working Electrode in Photoelectrochemical Cell. Journal of  
414 Xi'an Shiyou University, Natural Science Edition, 17 (2021) 305-316.

415 [29] Sutthipoj Wongrerkdee, Sasimonton Moungsrijun, Linking bridge improvement of  
416 ZnO/N719 interfaces via ammonia treatment for efficiency enhancement of dye-sensitized  
417 solar cell, Surfaces and Interfaces 23 (2021) 100991.

418 [30] Prakhar Shukla, Jitendra Kumar Shukla, Facile sol-gel synthesis and enhanced  
419 photocatalytic activity of the V<sub>2</sub>O<sub>5</sub>-ZnO nanoflakes, Journal of Science: Advanced Materials  
420 and Devices 3 (2018) 452-455.

421 [31]. Sourav Sadhukhan Tapas Kumar Ghosh Dipak Rana, Indranil Roy Amartya  
422 Bhattacharyya Gunjan Sarkar Mukut, Chakraborty Dipankar Chattopadhyay, Studies on  
423 synthesis of reduced graphene oxide (RGO) via green route and its electrical property,  
424 Materials Research Bulletin, 79 (2016) 41-51.

425 [32]. G. Nagaraju, Udayabhanu, Shivaraj, S.A. Prashanthb, M. Shastri, K.V. Yathish, C.  
426 Anupama, D. Rangappa, Electrochemical heavy metal detection, photocatalytic,  
427 photoluminescence, biodiesel production and antibacterial activities of Ag-ZnO nanomaterial,  
428 Materials Research Bulletin 94 (2017) 54–63.

429 [33]. Veena Ragupathi, Manukonda Madhu babu, Puspamitra Panigrahi and N. Ganapathi  
430 Subramaniam, Enhanced Electrical and Optical properties of Al doped and ZnO nanoparticles  
431 for Optoelectronic Application: Ecofriendly Green Route, IOP Publishing Journal of Physics:  
432 Conference Series 1495 (2020) 012040.

433 [34]. Nguyen Dien Kha Tu, Jaeyoo Choi, Chong Rae Park, and Heesuk Kim, Remarkable  
434 Conversion Between n- and p-Type Reduced Graphene Oxide on Varying the Thermal  
435 Annealing Temperature, Chem. Mater., 27 (2015) 7362–7369.

436 [35]. Y.-B. Tang, C.-S. Lee, J. Xu, Z. T. Liu, Z. Chen, Z. He, Y. L. Cao, G. Yuan, H. Song,  
437 L. Chen, Incorporation of Graphenes in Nanostructured TiO<sub>2</sub> Films via Molecular Grafting  
438 for Dye-Sensitized Solar Cell Application. ACS Nano, 4 (2010) 3482–3488.

439 [36]. N. Yang, J. Zhai, D. Wang, Y. Chen, L. Jiang, Two-Dimensional Graphene Bridges  
440 Enhanced Photoinduced Charge Transport in Dye-Sensitized Solar Cells. ACS Nano 4 (2010)  
441 887–894.

442 [37]. Artur Wiatrowski, Michał Mazur, Agata Obstarczyk, Damian Wojcieszak, Comparison  
443 of the Physicochemical Properties of TiO<sub>2</sub> Thin Films Obtained by Magnetron Sputtering  
444 with Continuous and Pulsed Gas Flow, Coatings 8 (2018) 412.

445 [38]. Alwin, S., Shajan, X.S., Karuppasamy, K., and Warriar, K.G.K. Microwave assisted  
446 synthesis of high surface area TiO<sub>2</sub> aerogels: A competent photoanode material for quasi-  
447 solid dye-sensitized solar cells. Mater Chem Phys, 196 (2017) 37–44.

448 [39]. Deepak, T.G., Anjusree, G.S., Pai, K.R.N., Subash, D., Nair, S. v, and Nair, A.S.  
449 Cabbage leaf-shaped two-dimensional TiO<sub>2</sub> mesostructures for efficient dye-sensitized solar  
450 cells. RSC Adv, 4 (51) (2014) 27084–27090.

451 [40]. Ren, J., Que, W., Yin, X., He, Y., and Javed, H.M.A. Novel fabrication of TiO<sub>2</sub>/ZnO  
452 nanotube array heterojunction for dye-sensitized solar cells. RSC Adv, 4 (15) (2014) 7454–  
453 7460.

- 454 [41]. Bhattacharya, S., and Datta, J. Wide-low energy coupled semi-conductor layers of  $\text{TiO}_2$   
455 –  $\text{CdX}$  boosting the performance of DSSC. *Solar Energy*, 208 (2020) 674–687.
- 456 [42]. Ansir, R., Ullah, N., Ünlü, B., Mujtaba Shah, S., and Özacar, M. Effect of annealing  
457 temperatures on performance of DSSCs fabricated using Ag or  $\text{Pd@C@ZnO}$  composites as  
458 photoanode materials. *Solar Energy*, 224 (2021) 617–628.
- 459 [43]. Ramarajan, R., Purushothamreddy, N., Dileep, R.K., Kovendhan, M., Veerappan, G.,  
460 Thangaraju, K., and Paul Joseph, D. Large-area spray deposited Ta-doped  $\text{SnO}_2$  thin film  
461 electrode for DSSC application. *Solar Energy*, 211 (2020) 547–559.
- 462 [44]. Khojasteh, F., Mersagh, M.R., and Hashemipour, H. The influences of Ni, Ag-doped  
463  $\text{TiO}_2$  and  $\text{SnO}_2$ , Ag-doped  $\text{SnO}_2/\text{TiO}_2$  nanocomposites on recombination reduction in dye  
464 synthesized solar cells. *J Alloys Compd*, 890 (2022) 161709.
- 465 [45]. Smok, W., Tański, T., Drygała, A., and Podwórny, J. Facile route to prepare hybrid  
466  $\text{TiO}_2\text{-SnO}_2$  DSSCs. *Appl Surf Sci*, 605 (2022) 154850.
- 467 [46]. Theerthagiri, J., Senthil, R.A., Arunachalam, P., Bhabu, K.A., Selvi, A., Madhavan, J.,  
468 Murugan, K., and Arof, A.K. Electrochemical deposition of carbon materials incorporated  
469 nickel sulfide composite as counter electrode for dye-sensitized solar cells. *Ionics* 2016 23:4,  
470 23 (4) (2016) 1017–1025.
- 471 [47]. Maiaugree, W., Tansoonton, T., Amornkitbamrung, V., and Swatsitang, E.  
472  $\text{Ni}_3\text{S}_2$ @MWCNTs films for effective counter electrodes of dye-sensitized solar cells. *Current*  
473 *Applied Physics*, 19 (12), (2019) 1355–1361.
- 474 [48]. Mirzaei, M., and Gholivand, M.B. Introduction of Pt-free counter electrode based on f-  
475 MWCNTs@ $\text{NiMoSe}_2$  nanocomposite for efficient dye-sensitized solar cells. *Solar Energy*,  
476 227 (2021) 67–77.

477 [49]. Ibrahim, A.S., Anbarasu, P., Mahendran, R., Rajendran, K., Sekhar, K.C., and Sathish,  
478 S. Facile synthesis of cobalt sulfide/carbon nanotube composites as a low-cost Pt-free counter  
479 electrode for dye-sensitized solar cells (DSSCs). *Diam Relat Mater*, 130 (2022) 109440.

480 [50]. Anto Feradrick Samson, V., Bharathi Bernadsha, S., Fennyl Britto, J., Victor Antony  
481 Raj, M., and Madhavan, J. Synthesis of rGO/NiFe<sub>2</sub>O<sub>4</sub> nanocomposite as an alternative  
482 counter electrode material to fabricate Pt-free efficient dye sensitized solar cells. *Diam Relat*  
483 *Mater*, 130 (2022) 109406.

484 [51]. Samson, V.A.F., Bernadsha, S.B., Paul Winston, A.J.P., Divya, D., Abraham, J., Raj,  
485 M.V.A., and Madhavan, J. rGO Sheets/ZnFe<sub>2</sub>O<sub>4</sub> Nanocomposities as an Efficient Electro  
486 Catalyst Material for I<sub>3</sub><sup>-</sup>/I<sup>-</sup> Reaction for High Performance DSSCs. *Journal of Inorganic and*  
487 *Organometallic Polymers and Materials* 32:3, 32 (3) (2022) 1183–1189.

488

489

490

491

492

493

494

495

496

497

498

499

500

501

502 **Figures**

503

504

505

506

507

508

509

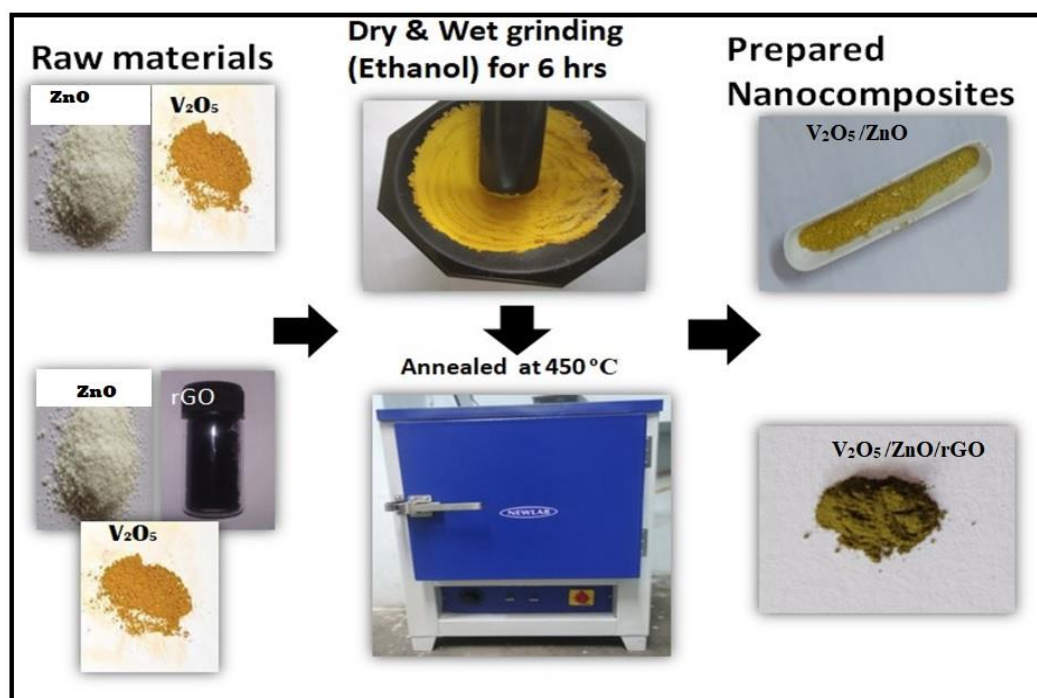
510

511

512

513

514



515 **Fig. 1. Schematic diagram of synthesis of nanocomposites.**

516

517

518

519

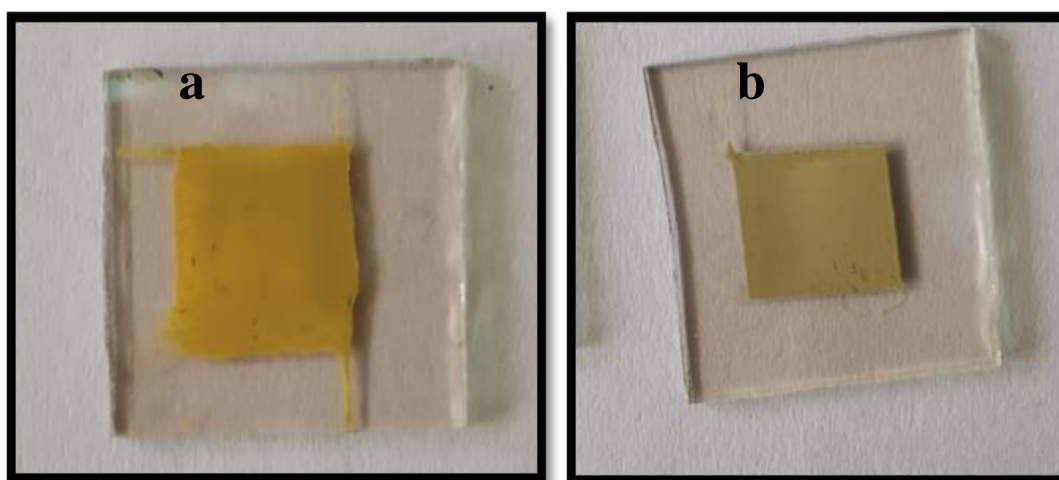
520

521

522

523

524



525 **Fig. 2. Prepared V<sub>2</sub>O<sub>5</sub>/ZnO and rGO-V<sub>2</sub>O<sub>5</sub>/ZnO photoanodes**

526

527  
528  
529  
530  
531  
532  
533  
534  
535  
536  
537  
538  
539  
540  
541  
542  
543  
544  
545  
546  
547  
548  
549  
550  
551

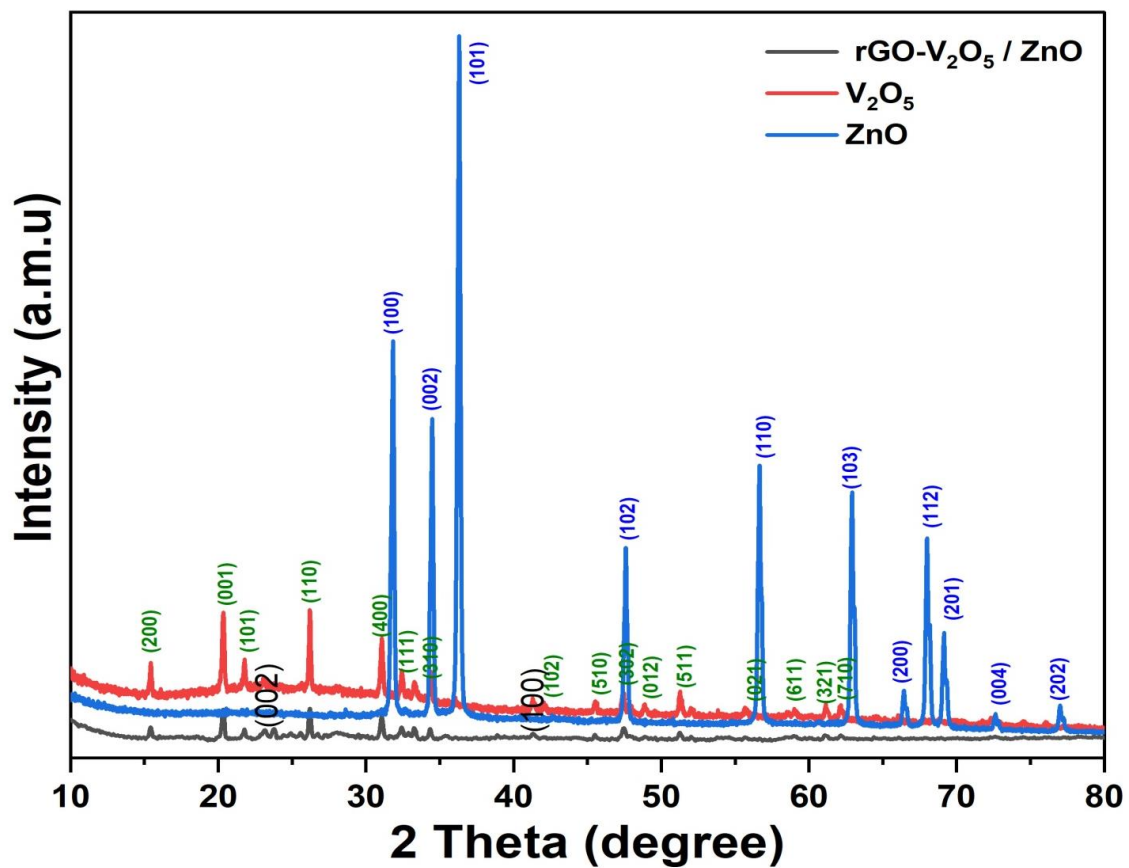
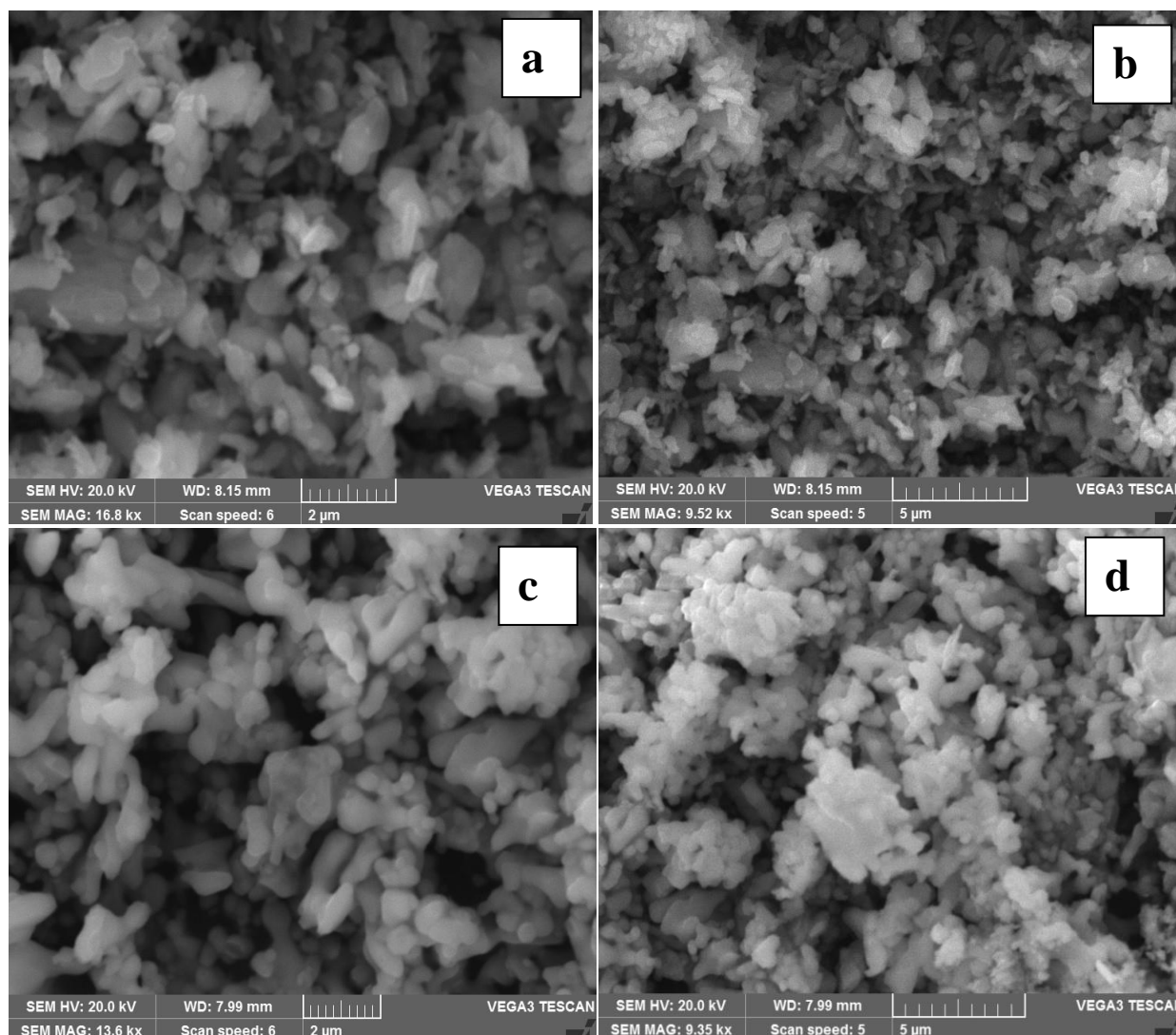


Fig. 3. XRD pattern of V<sub>2</sub>O<sub>5</sub>, ZnO and rGO-V<sub>2</sub>O<sub>5</sub>/ZnO NCs.

552  
553  
554  
555  
556  
557  
558  
559  
560  
561  
562  
563  
564  
565  
566  
567  
568  
569  
570  
571  
572  
573  
574  
575  
576



**Fig. 4. SEM Images of (a, b) 2 $\mu m$ , 5 $\mu m$  for  $V_2O_5/ZnO$  and (c,d) 2 $\mu m$ , 5 $\mu m$  for  $rGO-V_2O_5/ZnO$  nanocomposites.**

577

578

579

580

581

582

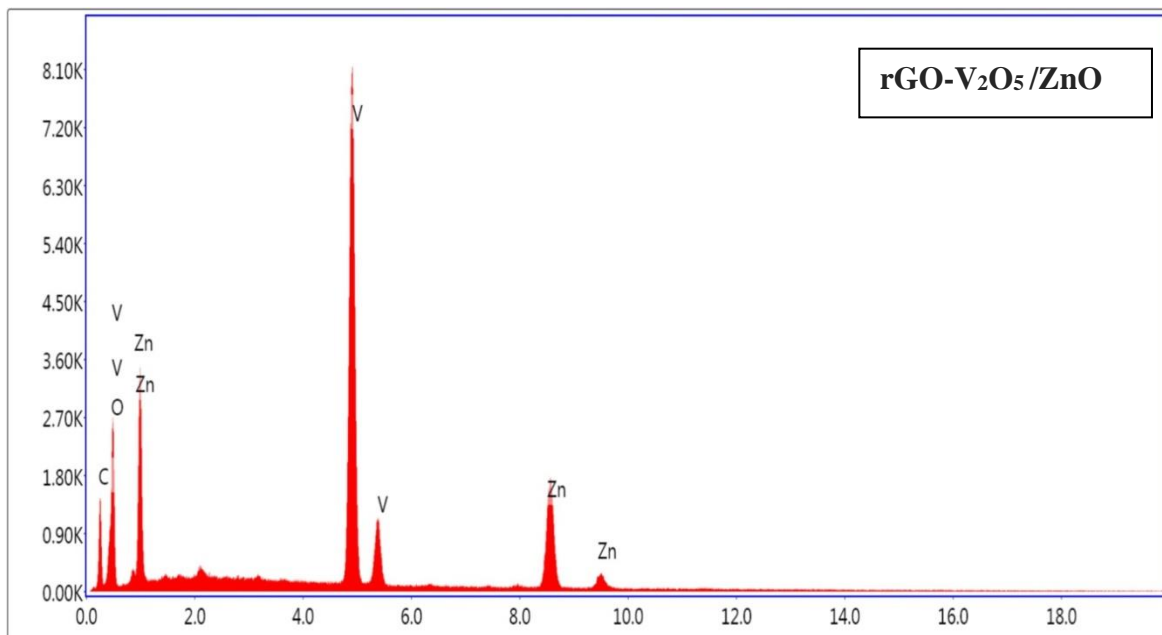
583

584

585

586

587



588

589

590

591

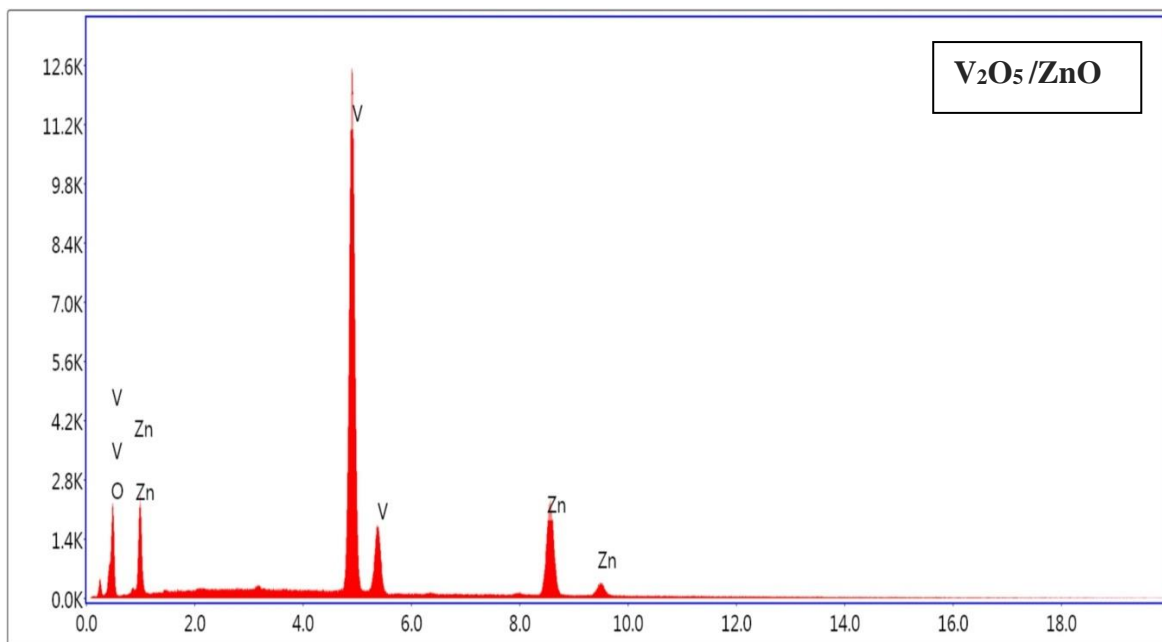
592

593

594

595

596



597

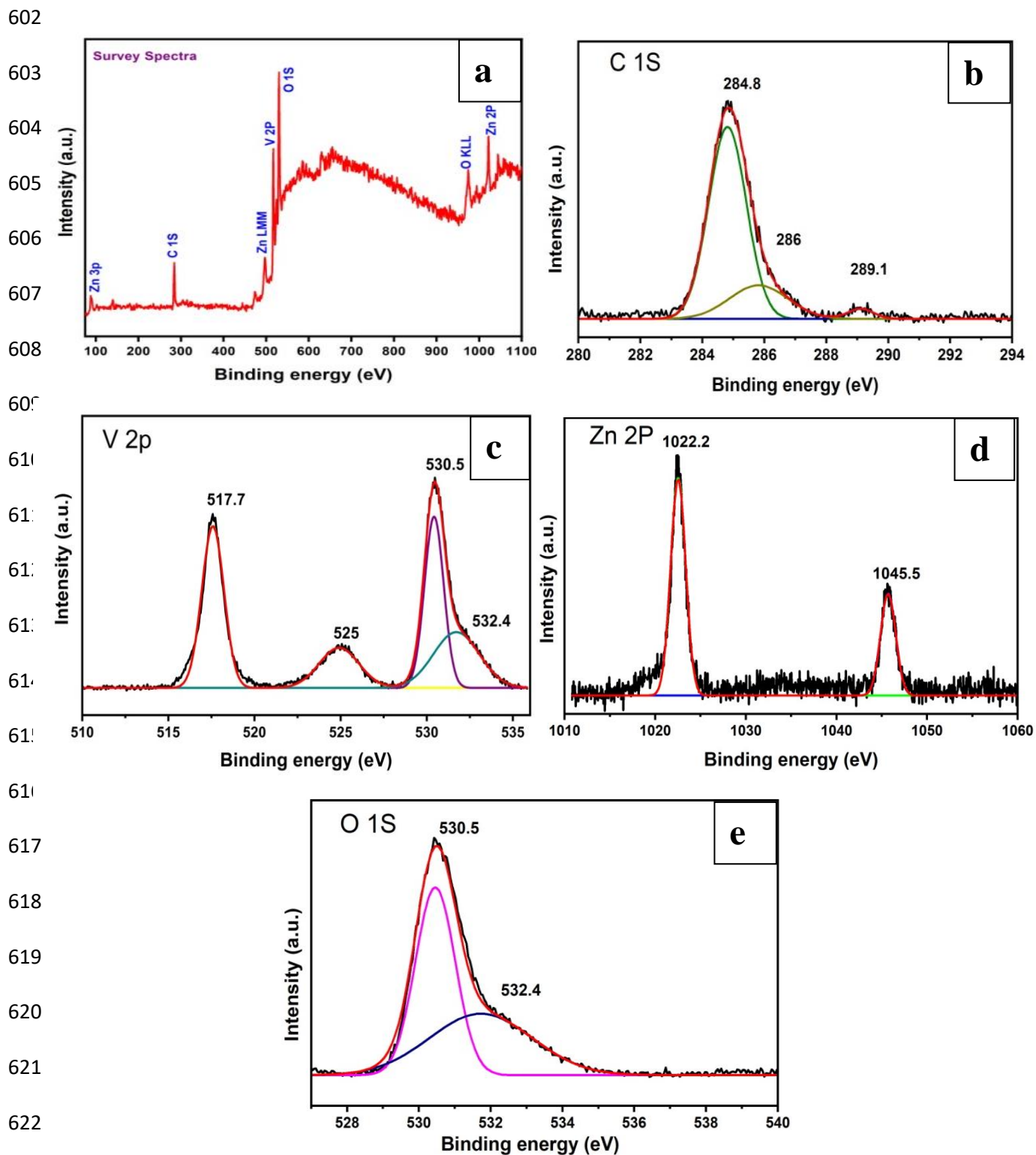
598 **Fig. 5. EDX images of rGO-V<sub>2</sub>O<sub>5</sub>/ZnO and V<sub>2</sub>O<sub>5</sub>/ZnO nanocomposites.**

599

600

601





624 **Fig. 6. (a) XPS Survey spectrum of rGO-V<sub>2</sub>O<sub>5</sub>/ZnO nanocomposites (b) C 1s peaks (c)**  
 625 **V 2p peaks (d) Zn 2p peaks (e) O 1s peaks.**

626

627  
628  
629  
630  
631  
632  
633  
634  
635  
636  
637  
638  
639  
640  
641  
642  
643  
644  
645  
646  
647  
648  
649  
650  
651

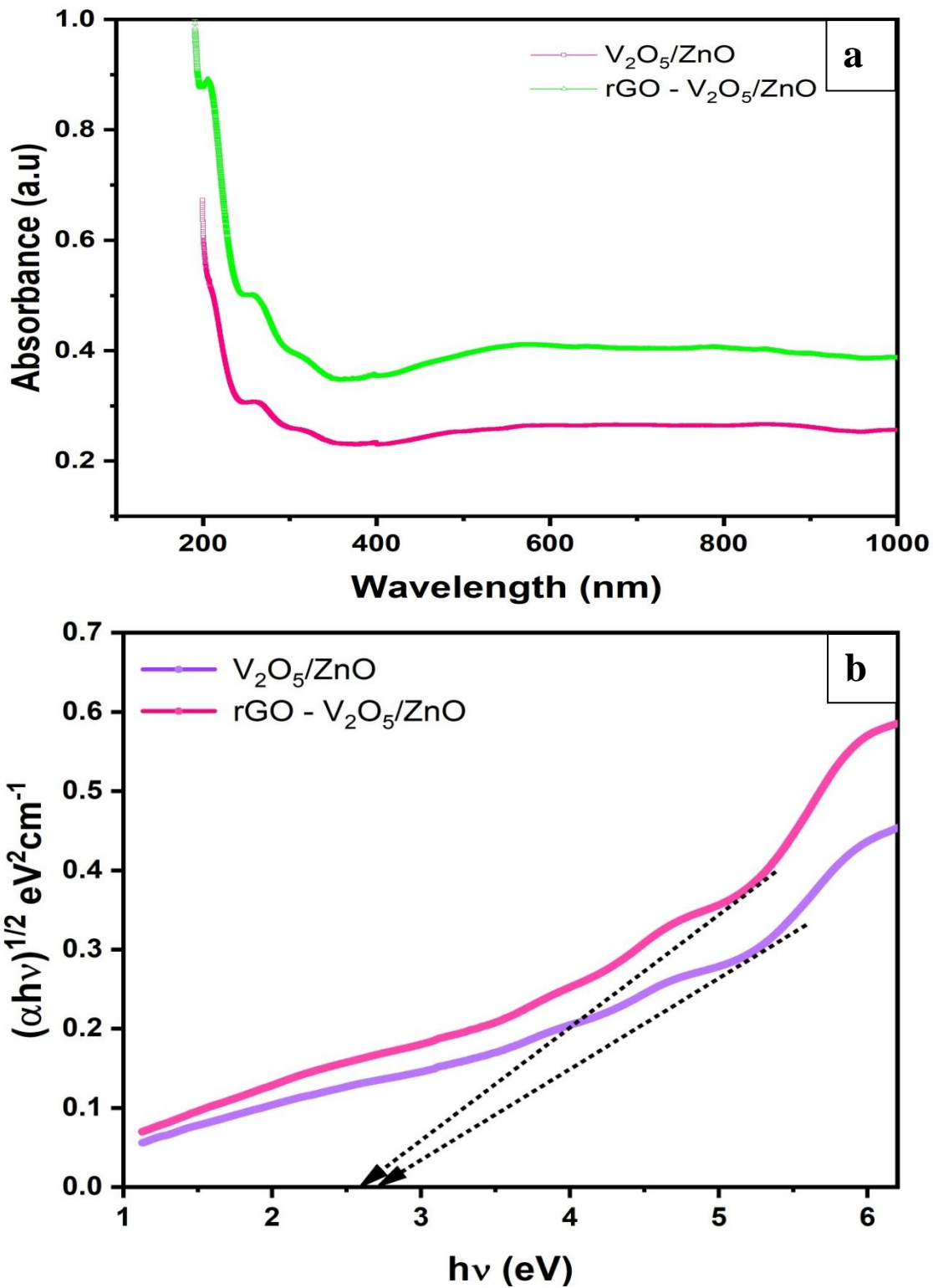
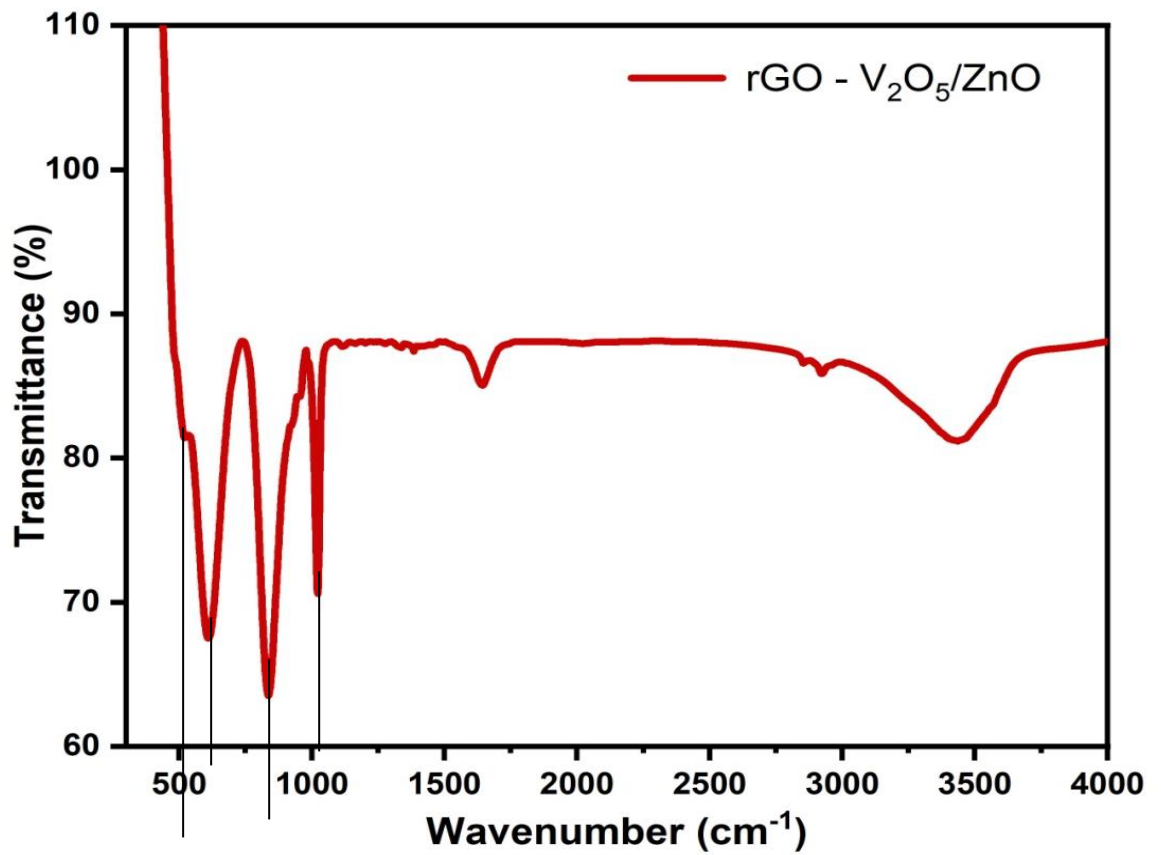


Fig. 7. UV absorption spectrum (a) and Tauc's Plot (b) for prepared nanocomposites.

652  
653  
654  
655  
656  
657  
658  
659  
660  
661  
662  
663  
664  
665  
666  
667  
668  
669  
670  
671  
672  
673  
674  
675  
676



**Fig. 8. FT-IR Spectrum of rGO-V<sub>2</sub>O<sub>5</sub>/ZnO nanocomposites**

677

678

679

680

681

682

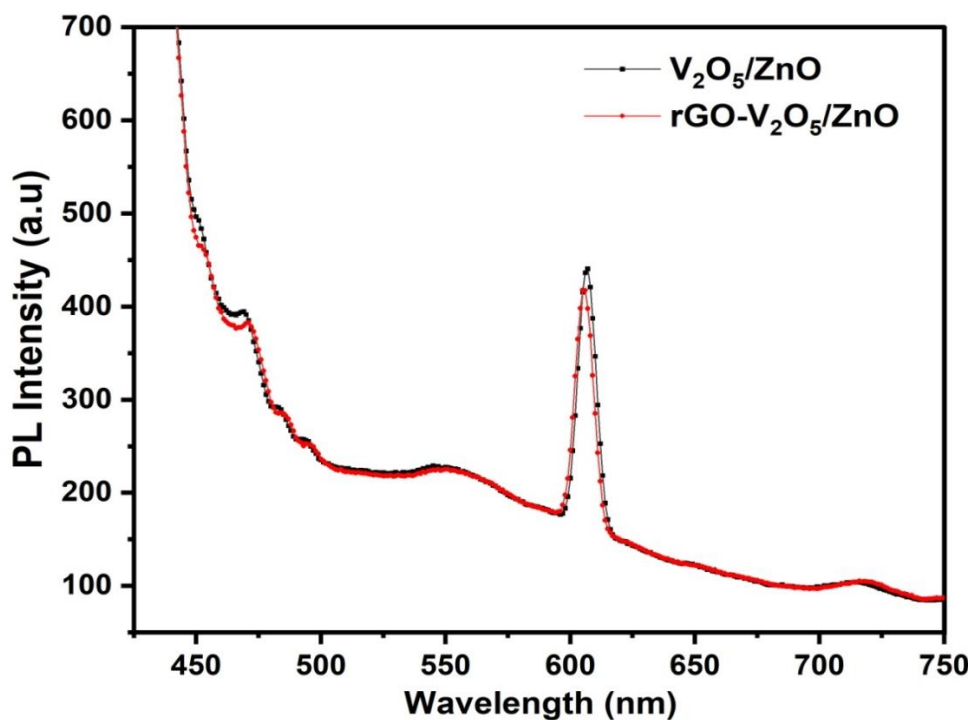
683

684

685

686

687



688 Fig. 9. Photoluminescence spectrum for prepared nanocomposites.

689

690

691

692

693

694

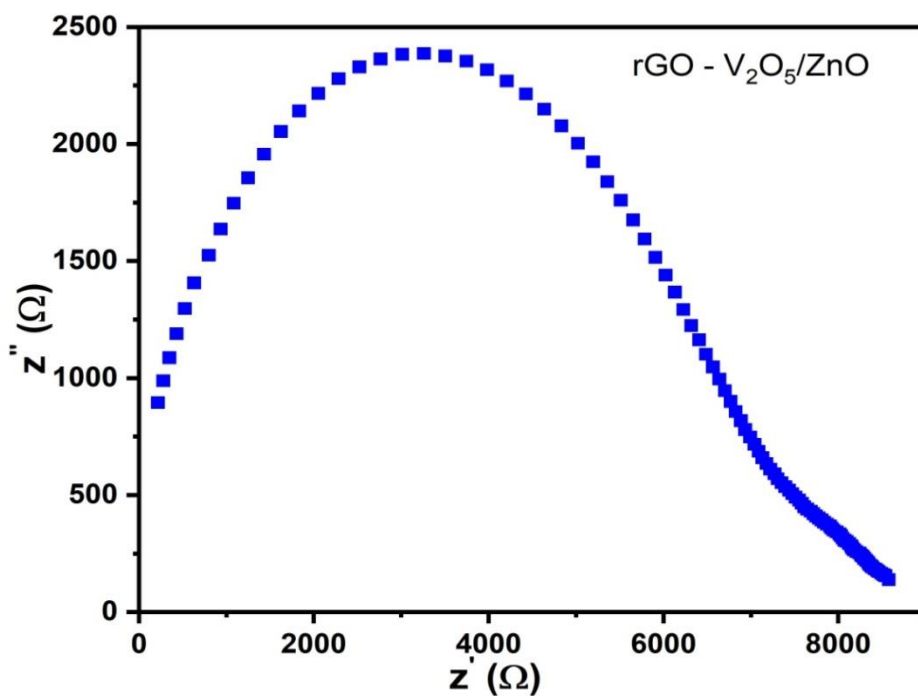
695

696

697

698

699



700 Fig. 10. Nyquist Plot of  $rGO-V_2O_5/ZnO$  nanocomposites.

701

702

703

704

705

706

707

708

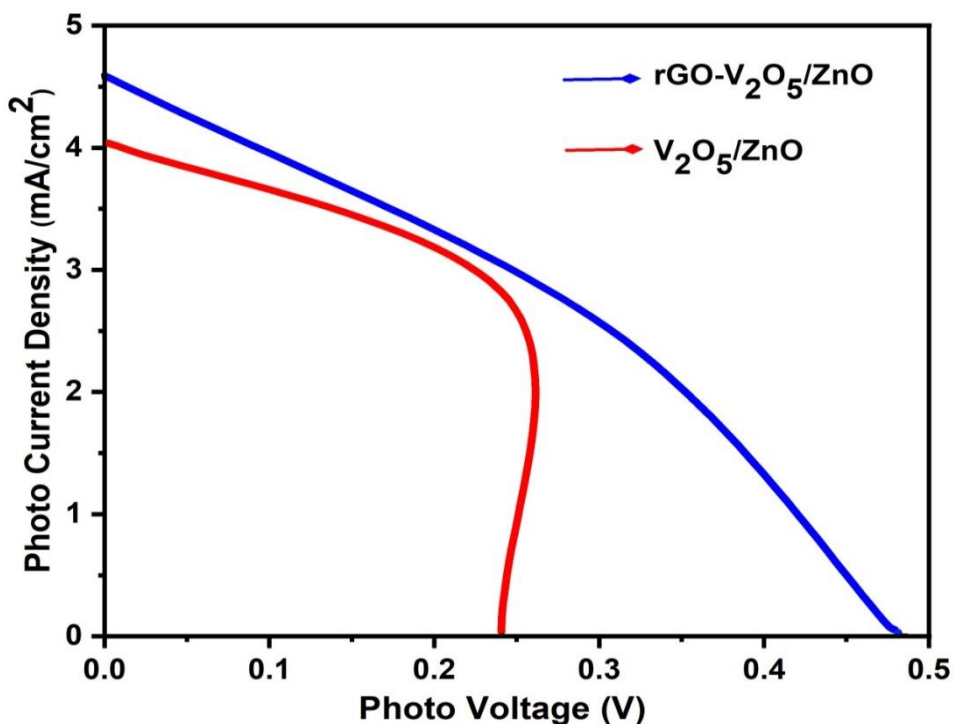
709

710

711

712

713



714 **Fig. 11.** J-V Characteristic curves of rGO-V<sub>2</sub>O<sub>5</sub>/ZnO nanocomposites photoanode based  
715 DSSCs.

716

717

718 **Table 1.** Hall Effect measurements of rGO-V<sub>2</sub>O<sub>5</sub>/ZnO NCs.

Sample	Type	Hall coefficient	n (cm <sup>-3</sup> )	μ (cm <sup>2</sup> V <sup>-1</sup> S <sup>-1</sup> )	ρ (Ωcm)	σ (Ω <sup>-1</sup> cm <sup>-1</sup> )
rGO -V <sub>2</sub> O <sub>5</sub> /ZnO	n	1.87 x 10 <sup>6</sup>	4.94 x 10 <sup>12</sup>	2375	1.82x10 <sup>-3</sup>	4.05x10 <sup>2</sup>

719

720

721

722

723 **Table 2.** Photoelectrochemical (PEC) Parameters for V<sub>2</sub>O<sub>5</sub>/ZnO and rGO-V<sub>2</sub>O<sub>5</sub>/ZnO DSSCs

724

Sample	J <sub>sc</sub> mA/cm <sup>2</sup>	V <sub>oc</sub> v	FF %	η %
V <sub>2</sub> O <sub>5</sub> /ZnO	4.028	0.245	0.72	0.715
rGO-V <sub>2</sub> O <sub>5</sub> /ZnO	4.64	0.461	0.58	1.201

725

726 **Table 3. Various Photoanode materials and their photoconversion efficiencies.**

727

Photoanode Material	Method	PCE (%)	Reference
TiO <sub>2</sub> aerogels	Sol gel	5.2	[38]
TiO <sub>2</sub> Nanoleaves	Anodization	8.5	[39]
TiO <sub>2</sub> /ZnO	Anodization	3.98	[40]
TiO <sub>2</sub> - CdX	Hydrothermal	13.3	[41]
Ag@C @ZnO	Hydrothermal	3.60	[42]
Ta-doped SnO <sub>2</sub>	Spray pyrolysis	3.36	[43]
Ag-doped SnO <sub>2</sub> /TiO <sub>2</sub>	Hydrothermal	6.93	[44]
TiO <sub>2</sub> -SnO <sub>2</sub>	hybrid sol-gel	4.96	[45]
NiS/AB (acetylene black)	Electrochemical deposition	6.75	[46]
Ni <sub>3</sub> S <sub>2</sub> @MWCNTs	Hydrothermal	7.48	[47]
f-MWCNTs@NiMoSe <sub>2</sub>	Hydrothermal	7.39	[48]
CoS <sub>2</sub> @MWCNT	Hydrothermal	8.85	[49]
rGO/NiFe <sub>2</sub> O <sub>4</sub>	Hydrothermal	8.41	[50]
rGO/ZnFe <sub>2</sub> O <sub>4</sub>	Hydrothermal	8.71	[51]

728